Determining material parameters using phase-field simulations and experiments

Zhang, Jin; Poulsen, Stefan O.; Gibbs, John W.; Voorhees, Peter W.; Poulsen, Henning Friis

Published in:
Acta Materialia

Link to article, DOI:
10.1016/j.actamat.2017.02.056

Publication date:
2017

Document Version
Publisher's PDF, also known as Version of record

Acta Materialia 129 (2017) 229–238

Contents lists available at ScienceDirect

Acta Materialia

journal homepage: www.elsevier.com/locate/actamat

Full length article

Determining material parameters using phase-field simulations and experiments

Jin Zhang [a], Stefan O. Poulsen [b], John W. Gibbs [c], Peter W. Voorhees [b], Henning F. Poulsen [a, *]

[a] NEXMAP, Department of Physics, DTU, 2800, Kongens Lyngby, Denmark
[b] Department of Materials Science and Engineering, Northwestern University, Evanston, IL, 60208, USA
[c] Materials Science and Technology Division, Los Alamos National Laboratory, Los Alamos, USA

ARTICLE INFO

Article history:
Received 7 November 2016
Received in revised form
23 January 2017
Accepted 20 February 2017
Available online 22 February 2017

Keywords:
Phase-field method
X-ray tomography
Coarsening
Al alloys
Temporal evolution

ABSTRACT

A method to determine material parameters by comparing the evolution of experimentally determined 3D microstructures to simulated 3D microstructures is proposed. The temporal evolution of a dendritic solid-liquid mixture is acquired in situ using x-ray tomography. Using a time step from these data as an initial condition in a phase-field simulation, the computed structure is compared to that measured experimentally at a later time. An optimization technique is used to find the material parameters that yield the best match of the simulated microstructure to the measured microstructure in a global manner. The proposed method is used to determine the liquid diffusion coefficient in an isothermal Al-Cu alloy. However, the method developed is broadly applicable to other experiments in which the evolution of the three-dimensional microstructure is determined in situ. We also discuss methods to describe the local variation of the best-fit parameters and the fidelity of the fitting. We find a liquid diffusion coefficient that is different from that measured using directional solidification.

1. Introduction

Computational methods play an important role in accelerating the discovery and development of advanced materials [1]. One of the most promising areas in which computational methods are employed is in Integrated Computational Materials Engineering (ICME), which is receiving increased attention from both academia and industry [2,3]. The establishment of reliable and comprehensive materials databases - the main component of the Materials Genome Initiative (MGI) [3] - is a key to the success of ICME [2,4]. Traditionally, material parameters are measured one at a time by designing dedicated experiments using idealized specimens and specimen geometries (e.g. a planar interface in a diffusion couple experiment for measuring the diffusion coefficient). However, such procedures are often tedious, and typically parameters are measured only in a fraction of the relevant phase space, which may involve materials composition, temperature, pressure, etc. In addition, the idealized geometry may not be representative: industrially relevant microstructures are heterogeneous and artificial surfaces may introduce unwanted boundary effects. Furthermore, for hierarchically ordered materials, effects on different length scales compete and interact. Recently, researchers have begun to calculate material parameters from first-principles, such as the free energy [5] and the diffusion coefficients in the solid phase [6–8] and the liquid phase [9]. However, experimental verification of the calculated material parameters under realistic conditions is needed.

In this work, we propose to determine material parameters directly from structural studies of bulk samples acquired during synthesis or processing. To image material microstructure evolution, various techniques have been used, e.g. Computed Tomography (CT) [10,11], 3D X-Ray Diffraction (3DXRD) [12] and Diffraction Contrast Tomography (DCT) [13]. Using x-rays emitted from a synchrotron source, time-resolved high spatial resolution 3D images can be acquired using tomographic methods, for a review see Ref. [14]. In favorable cases, the temporal resolution may be on the sub-second scale [15]. Some of these techniques are increasingly becoming available in laboratory sources, such as the laboratory-based DCT (labDCT) [16]. At the same time, the rapid increase in computing power and the development of advanced modeling

* Corresponding author.
E-mail address: hfpo@fysik.dtu.dk (H.F. Poulsen).

http://dx.doi.org/10.1016/j.actamat.2017.02.056

techniques such as quantitative phase-field models [17–20], accurate simulations of microstructure evolution in 3D have become feasible. Therefore, we propose to determine material parameters by direct comparison between the 3D temporal evolution of microstructures determined through experiment and phase-field simulation. We claim that the parameter values that provide the best match between the experimental and the simulated microstructure in a global manner (both in 3D space and in time) correspond to the physically correct ones. The proposed method can be used to verify the calculated material parameters by first-principles and multiscale modeling simulations. Another advantage of this approach is that it permits the measurement of multiple - in some cases potentially all relevant - material parameters from one experiment in a realistic environment. Notice that though this paper focuses on the phase-field method, other modeling techniques relevant to the problem studied can also be used, such as Monte Carlo Potts model [21] and the vertex model [22] for grain growth and the level-set method for solidification [23].

In recent years, several direct comparisons between experiment and phase-field simulations have been performed [24–27], but the comparisons have mainly been qualitative or based on average quantities, such as the average particle size and the interface area per unit volume. Rigorous comparisons of the morphologies are rare. McKenna et al. [25] used a one-to-one comparison to test a grain growth phase-field model, but they did not use it for extracting material parameters. Demirel et al. [28] used a similar approach for grain growth in thin films. Aagesen et al. [24] estimated a value of the liquid diffusion coefficient using a comparison between phase-field simulations and tomography in a heuristic manner. We here introduce a general optimization formalism and discuss key aspects of this fitting approach, such as the cost functions to quantify the similarity between experiment and simulation, the accuracy, the initial and boundary conditions and the computational speed. To the best of our knowledge, this is the first systematic study where phase-field simulations and 3D tomography are combined to extract material properties. Though in general the optimization relies on performing phase-field simulations many times, we predict that one may only need to consider a small fraction of space-time in a given step of the optimization for many relevant problems.

We demonstrate the approach by fitting the liquid diffusion coefficient D^{L} and the capillary length l^{L} in the context of the isothermal coarsening of dendrites in a liquid of composition nearly equal to that of the eutectic composition in the Al-Cu system. It is a well-studied system, and relevant material parameters have been extensively measured by traditional means, e.g. the free energy [29,30], the solid/liquid interfacial energy [31,32] and the liquid diffusion coefficient [33–35]. However, the values determined from the liquid diffusion coefficient measurements display a large scatter in value, argued to be mainly due to convection [33]. Moreover, an existing temperature gradient during directional solidification may alter the measured liquid diffusion coefficient. In section 2, the fitting methodology is presented in detail. In section 3, the results of the demonstration on the Al-Cu system are provided. We discuss limitations and potential applications in section 4 and conclude the paper in section 5.

2. Optimization approach

Initially, we present the mathematical model and the associated terminology and notations. Then two types of cost functions and several ways to define the fitting domain are proposed and compared. Finally, the statistics of the fitting method is discussed. Throughout, for reasons of simplicity, we shall assume a two-phase problem, where the microstructure is characterized by a moving boundary between the two phases.

2.1. The mathematical model

The fitting approach is shown schematically in Fig. 1. Here the symbol $\mathscr{G}$ represents the geometry of the material microstructure. The x-ray experiment provides a series of 3D material microstructures $\mathscr{G}^{\mathrm{exp}}(t)$ evolving with time (shown in the upper solid box in Fig. 1). With one frame of the experimental microstructure (time t_0) as input ($\mathscr{G}^{\mathrm{sim}}(t_0) = \mathscr{G}^{\mathrm{exp}}(t_0)$) and a guess of material parameters $\mathbf{p}$, the simulation method [19] can produce a series of evolving microstructures $\mathscr{G}^{\mathrm{sim}}(t, \mathbf{p})$ (shown in the lower dashed box in Fig. 1). For time $t > t_0$, a cost function f_{cost} is used to measure the dissimilarity between the two microstructures. We claim the real material parameters $\mathbf{p}^{\mathrm{real}}$ should give the least dissimilarity between the experimental and simulated microstructures, i.e. f_{cost} reaches a minimum as shown in Fig. 1 (right).

This fitting process can be described by the following optimization problem:

$$\begin{aligned} \text{find} \quad & \mathbf{p} \\ \text{minimize} \quad & f_{\mathrm{cost}}(t, \mathbf{p}) = f_{\mathrm{cost}}\Big(\mathscr{G}^{\mathrm{exp}}(t), \mathscr{G}^{\mathrm{sim}}(t, \mathbf{p})\Big) \\ \text{such that} \quad & \mathscr{G}^{\mathrm{sim}}(t, \mathbf{p}) \text{ fulfills phase-field equation} \\ & \mathscr{G}^{\mathrm{sim}}(t_0, \mathbf{p}) = \mathscr{G}^{\mathrm{exp}}(t_0) \\ & \mathscr{G}^{\mathrm{sim}}(t, \mathbf{p}) \text{ fulfills boundary condition} \end{aligned} \tag{1}$$

The optimization problem can be solved by any appropriate optimization algorithm. Notice here the optimization approach is independent of the geometric representation $\mathscr{G}$, which may thus be discretized like a binary image or be continuous like NURBS (explicit) [36] and level-set methods (implicit) [37]. The flowchart of the fitting algorithm is shown in Fig. 2.

2.2. The cost function

Two types of cost functions are proposed based on the representation of the microstructure geometry. If these microstructures are represented by binary images ($\mathscr{G}^{\mathrm{exp}} = \mathrm{Img}^{\mathrm{exp}}$, $\mathscr{G}^{\mathrm{sim}} = \mathrm{Img}^{\mathrm{sim}}$), the correlation function can be used to construct the cost function (the corr-cost function)

$$f_{\mathrm{cost}}(t, \mathbf{p}) = 1 - \underset{\Omega_{\mathrm{fit}}}{\mathrm{corr}}\Big(\mathrm{Img}^{\mathrm{exp}}(t), \mathrm{Img}^{\mathrm{sim}}(t, \mathbf{p})\Big) \tag{2}$$

where Ω_{fit} is the fitting domain. If a continuous geometry representation like the signed distance function as known from the level-set method is used ($\mathscr{G}^{\mathrm{exp}} = \phi^{\mathrm{exp}}$, $\mathscr{G}^{\mathrm{sim}} = \phi^{\mathrm{sim}}$), the squared 2-norm function can be used:

$$f_{\mathrm{cost}}(t, \mathbf{p}) = \frac{\left\|\phi^{\mathrm{sim}}(t, \mathbf{p}) - \phi^{\mathrm{exp}}(t)\right\|^2_{2,\Omega_{\mathrm{fit}}}}{\left\|\phi^{\mathrm{exp}}(t) - \phi^{\mathrm{exp}}(t_0)\right\|^2_{2,\Omega_{\mathrm{fit}}}} \tag{3}$$

Here, the normalization is used to make the cost function independent of the fitting domain size. By this definition, $\sqrt{f_{\mathrm{cost}}}$ has a physical meaning, namely representing the root mean square migration distance of the simulated interfaces relative to the experimentally determined interfaces if no topological change occurs. As the segmentation applied to the tomographic data in the example case given in the current work is based on the signed distance function [38], ϕ^{exp} is available. However, ϕ^{sim} is not directly available from the phase-field simulation. In this work, the equilibrium profile of a planar interface is used to provide an approximation of the signed distance function from the interpolation function in the phase-field model, and then a reinitialization

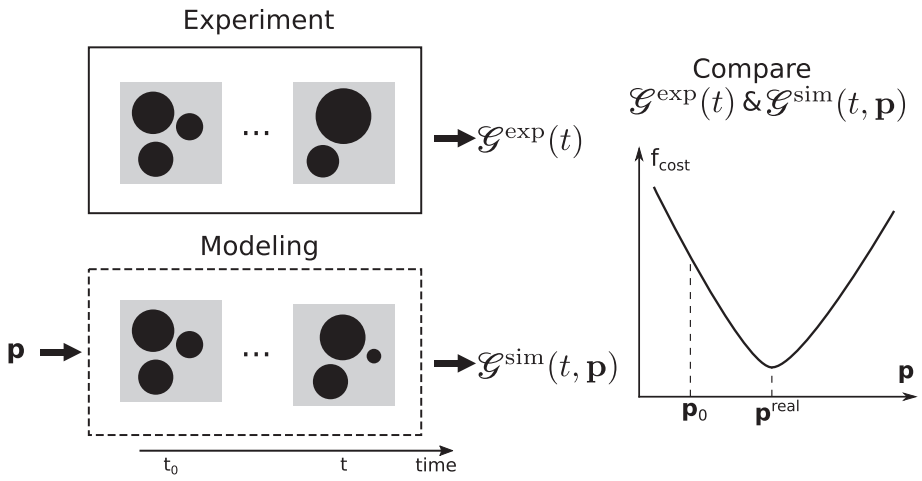

Fig. 1. Schematic diagram of the fitting method.

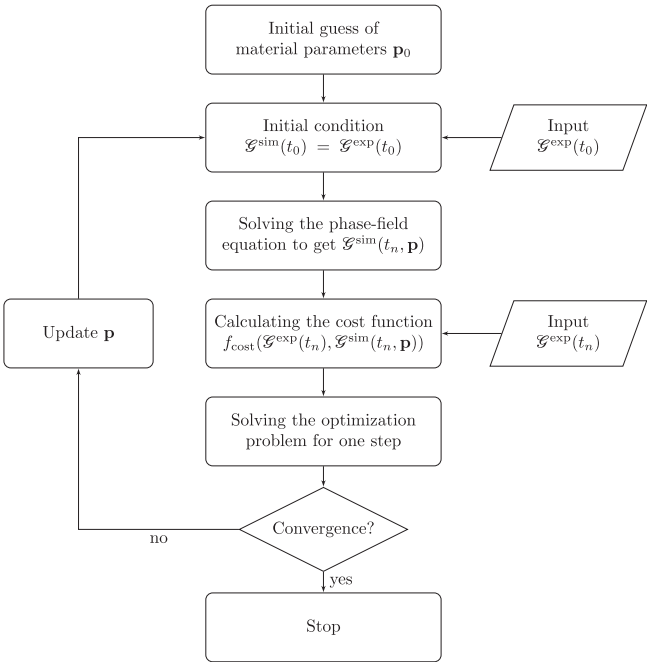

Fig. 2. Flowchart of the fitting algorithm.

algorithm [39] is used to calculate the signed distance function while leaving the interface position unchanged.

2.3. The fitting domain

We anticipate that a proper fitting domain Ω_{fit} often will be critical for the fitting. In particular, we need to remove regions which provide noisy or even wrong information on the underlying interfacial evolution due to known limitations of the applied model, such as missing physics or violated assumptions.

In the current work, we use an implicit representation of the microstructure. As the comparison of microstructures is only needed at the interfaces, regions far from the interface are removed from fitting. This also helps to reduce the computational cost. In this work, we restrict the fitting to an interfacial domain $\Omega_{\text{interface}}$; see the region between two dashed lines in Fig. 3. The interfacial domain with width w is defined as

$$\Omega_{\text{interface}=w} = \left\{\mathbf{x} : |\phi^{\exp}(\mathbf{x})| \leqslant \frac{w}{2}\right\} \tag{4}$$

where $\phi^{\exp}$ is the signed distance function of the experimental interface. We find that the cost function is insensitive to the width w when w is small, so in the current work $w = 5$ grid points will be used throughout.

A region near the boundary of the simulation domain is removed from the fitting domain. To reduce the computational cost, the simulation domain Ω^{sim} is usually chosen to be a subset of the sample. Artificial boundary conditions are imposed on the boundary of Ω^{sim}. In the region close to the external boundary of Ω^{sim}, we will not expect simulation to match experiment because of the assumed boundary condition. To overcome this problem, the fitting is constrained to a smaller subdomain Ω_{sub}, with size k, defined as

$$\Omega_{\text{sub}=k} = \left\{\mathbf{x} : |x_i - x_i^c| \leqslant \frac{k}{2}, i = 1,2,3\right\} \tag{5}$$

where $\mathbf{x}^c$ is the center of Ω^{sim} (see Fig. 3). The subdomain size k plays an important role in the fitting and will be discussed in detail

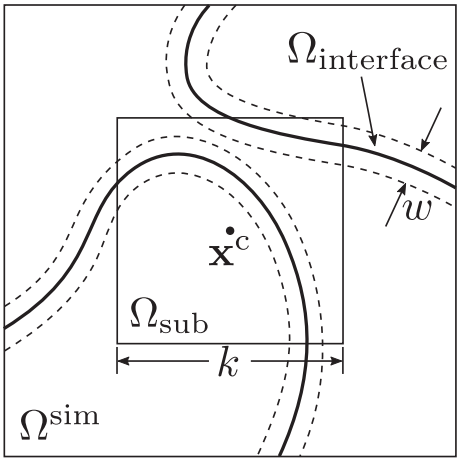

Fig. 3. Schematic diagram of the fitting domain. The thick lines show the interfaces; the simulation domain Ω^{sim} is where the phase-field simulation is performed; the subdomain Ω_{sub} is a smaller domain inside Ω^{sim} with size k; the interfacial domain $\Omega_{\text{interface}}$ is a narrow region with width w near the interface.

in section 3.4.2.

In some applications, there are regions with small features which are difficult to capture by simulation with a reasonable computational cost. In relation to the coarsening study below, there are regions where solid particles are separated by thin liquid films, as shown in Fig. 4. These films are too thin be resolved using the interface thickness employed in the phase-field simulation, so solid particles in close vicinity tend to coalesce in the simulations, which leads to a high local interface velocity. We can either reduce the grid size or exclude these regions. As these regions are not necessary for determining the liquid diffusion coefficient and it is more efficient to look at larger volumes that do not contain these small features than it is to refine the mesh significantly, these high-velocity regions will be removed from the fitting domain.

2.4. Statistics

Differences between experiment and simulation may arise from numerous sources, such as temperature gradients in the experiment, reconstruction and segmentation error, local fluctuation in the material parameters and discretization error in the simulation. These errors are often stochastic in nature. We hypothesize that one can reduce these errors by using a large number of interface patches in the fitting. Below we test this hypothesis as part of a systematic study of the importance of varying a number of settings of relevance to the fitting: the number of interface patches used, the size and position of the simulation domain Ω^{sim} and various combinations of starting time t_0 and fitting time t_n.

3. Application: coarsening of a hypo-eutectic Al-Cu system

In this section, the fitting methodology proposed in section 2 is applied to the coarsening of a hypo-eutectic Al-Cu system with a composition of 20 wt% Cu (calculated from the measured phase volume fraction). Firstly, the x-ray experiment, the setup of simulations and the fitting algorithm specific to this system are presented. Then we make a one-parameter fit to the liquid diffusion coefficient only, as it is the simplest case for fitting and easy for visualization and analysis. Finally, to demonstrate the generality of the fitting method, a two-parameters fit to both the liquid diffusion coefficient and the capillary length is given in section 3.5.

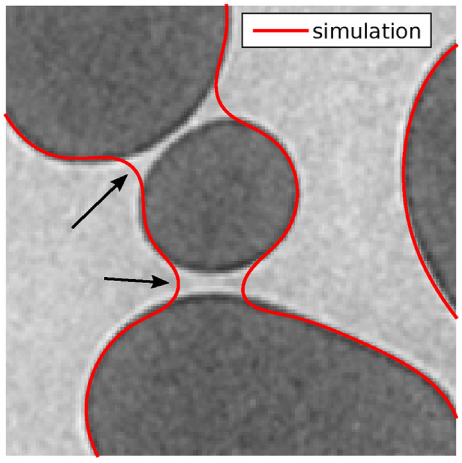

Fig. 4. Illustration of thin liquid films that are present in the microstructure. The simulation result (red curve) overlaid on the experimental data. The arrows show the regions of thin liquid films where coalescence occurs in the simulation. (For interpretation of the references to colour in this figure legend, the reader is referred to the web version of this article.)

3.1. X-ray tomography experiment

The experimental data used in this paper are phase contrast tomography data collected at the beamline TOMCAT at the Swiss Light Source. An isothermal coarsening experiment was performed for 362 min at a fixed temperature of $558^\circ C$, $5^\circ C$ above the eutectic temperature. The tomography data were reconstructed and segmented to provide a 3D movie of the microstructure evolution. The spatial and temporal resolutions are $\Delta x = 1.44\,\mu m$ and $\Delta t^{\text{exp}} = 231\,s$, respectively. Details about the experiment, reconstruction and segmentation can be found in Refs. [40–42].

3.2. Setup of phase-field simulation

To model coarsening of the Al-Cu system, multiorder-parameter models [43] or multiphase-field models [44] can be used. In the current work, the multiorder-parameter model presented in Refs. [43,45–47] with the interpolation function introduced in Ref. [19] is used. The total free energy of the system is expressed as a functional of phase-field variables (η_S and η_L) and Cu compositions (c_S and c_L) for each phase

$$F = \int_{\Omega^{\text{sim}}} \left(m \left[\sum_{i=\text{S,L}} \left(\frac{\eta_i^4}{4} - \frac{\eta_i^2}{2} \right) + \gamma \eta_S^2 \eta_L^2 + \frac{1}{4} \right] + \frac{\kappa}{2} \sum_{i=\text{S,L}} \left(\vec{\nabla} \eta_i \right)^2 + h^S f^S + h^L f^L \right) \mathrm{d}V \tag{6}$$

The evolution of the system is governed by the phase-field equations

$$\frac{\partial \eta_i}{\partial t} = -L \frac{\delta F}{\delta \eta_i}, \quad i = \text{S, L} \tag{7}$$

$$\frac{\partial c_i}{\partial t} = \vec{\nabla} \cdot \left(M_i \vec{\nabla} \frac{\delta F}{\delta c_i} \right), \quad i = \text{S, L} \tag{8}$$

Furthermore, appropriate initial conditions for $\eta_i(t = 0, \mathbf{x})$ and $c_i(t = 0, \mathbf{x})$ and boundary conditions for $\eta_i\left(t, \mathbf{x}\big|_{\partial\Omega^{\text{sim}}}\right)$ and $c_i\left(t, \mathbf{x}\big|_{\partial\Omega^{\text{sim}}}\right)$ are needed to guarantee a well-posed problem. The last two terms in Eq. (6) represent the bulk free energy density, which is constructed by interpolating the free energy densities of different phases (f^S and f^L) with the interpolation functions (h^S and h^L) of the form

$$h^S = \frac{\eta_S^2}{\eta_S^2 + \eta_L^2}, \quad h^L = \frac{\eta_L^2}{\eta_S^2 + \eta_L^2} \tag{9}$$

The mobilities (M_S and M_L) are related to the diffusion coefficients (D^S and D^L) by

$$M_S = \frac{D^S}{\frac{\partial^2 f^S}{\partial c_S^2}}, \quad M_L = \frac{D^L}{\frac{\partial^2 f^L}{\partial c_L^2}} \tag{10}$$

For further details on the model parameters (m,γ,κ and L) and their connection to the material parameters, and the calculation of functional derivatives in Eqs. (7) and (8), the reader can refer to [19].

The simulation domain size is chosen to provide a sufficient amount of interface patches for accurate fitting while keeping an affordable computational cost. In the one-parameter fitting in section 3.4, a simulation domain of $300 \times 300 \times 300$ voxels is used.

In the two-parameters fitting in section 3.5, a simulation domain of $400 \times 400 \times 400$ voxels is used. To discretize the phase-field equations, the second-order finite difference is used for the spatial discretization and the forward Euler method is used for the temporal discretization. For details on solving the phase-field equations with the finite difference method, the reader can refer to e.g. Ref. [48] for more information. The interface width l is chosen to be seven grid points, where the width of one voxel is equal to the grid spacing. The code is written in C and uses MPI to parallelize over multiple nodes. At the beginning of the experiment, there are features with high curvatures and the spatial resolution is not high enough to capture them; therefore the very first time steps are not used. Unless otherwise mentioned, the simulations are started with the experimental time step $t_0 = 10$ and the fitting is performed at later time steps, e.g. $t_n = 11, 12, \cdots, 15$.

3.2.1. Material parameters

In the current work, a parabolic free energy density function is used by fitting to the CALPHAD free energy [29]: $f^S = 2.78(c^S - 0.78)^2 - 4.61\, J/m^3$ and $f^L = 5.10(c^L - 0.57)^2 - 4.45\ J/m^3$. The capillary length of the liquid phase is $l^L = 0.63\ nm$, which is calculated from the Gibbs-Thomson coefficient measured in Ref. [31]. The initial guess of the diffusion coefficient is $D_0^L = 1 \times 10^{-9}\ m^2/s$. The anisotropy of the solid-liquid interfacial energy in Al-Cu is 0.0098 [49], which is small for coarsening, so we assume isotropic interfacial energy in this work. The diffusion coefficient in the solid is estimated to be four orders of magnitude less than in the liquid [50] and is therefore taken to be zero: $D^S = 0$. The anti-trapping current [18,51] is neglected in this work because the solute trapping effect of the problem studied is negligible: $Vl/D^L \sim \mathcal{O}(10^{-5}) \ll 1$, where V is the interface velocity and l is the interface width in the phase-field calculation, which is around $10\mu m$ in this work. The phase-field method is known to only reproduce the accepted sharp interface predictions when the product of the interface width and the mean curvature is small, $l\mathcal{K} \ll 1$ [52], so regions where this assumption is invalidated should be removed from the fitting domain. Regions of high curvature occur, for example, at topological singularities where there is pinching or merging of solid domains. However, in this case the high-curvature region is always related to the high-velocity region. In this work, the high-velocity region is removed, and the high curvature regions are not considered explicitly.

3.2.2. Initial condition

The initial condition for the phase-field variables (η_S and η_L) is input directly from experiment (use ϕ^{exp}), but the initial condition for the diffusion fields (c_S and c_L) is unknown as the small variations in liquid composition occurring during coarsening are undetectable with the current experimental method. Thus, the phase compositions are initially set to their equilibrium values. Numerical simulation shows that the initial relaxation caused by this artificial initial condition is fast and the change of volume fraction is much smaller than that in the experiment; therefore we assume the uncertainty related to the initial diffusion field will not influence the results of the fitting.

3.2.3. Boundary conditions

In the current work, a no-flux boundary condition is used in the one-parameter fitting in section 3.4 and a periodic boundary condition is used in the two-parameters fitting in section 3.5. As expected, both types of boundary conditions give rise to problems near the simulation domain boundary. The influence of the boundary condition will be studied in section 3.4.2 by varying the subdomain size.

3.3. Fitting method

As shown in Fig. 2, the phase-field equations need to be solved in each iteration, which makes the fitting process quite time-consuming. However, for the case of determining the diffusion coefficient only, the fitting can be done with only one phase-field simulation. This is based on the scaling property of the governing phase-field equations [19]:

$$\mathscr{G}^{\mathrm{sim}}\left(t, \alpha D^L\right) = \mathscr{G}^{\mathrm{sim}}\left(\alpha t, D^L\right) \tag{11}$$

where α is an arbitrary positive constant. So we only need to run the simulation once with an arbitrary value of the diffusion coefficient to determine the cost function for other values of the diffusion coefficient through above scaling to the simulation time. A spline interpolation is used to interpolate the curve of f_{cost} over D^L since the simulations only produce output at discrete times. A standard nonlinear optimization algorithm is used to find the optimal D^L. The convergence criteria is that the derivative of the cost function is less than 1×10^{-6} in the current work.

3.4. One-parameter fitting: liquid diffusion coefficient

In this first case, all material parameters except the liquid diffusion coefficient are assumed to be known. Thus the only fitting variable is $\mathbf{p} = \{D^L\}$.

3.4.1. Test of the fitting with a small interface patch

To demonstrate the proposed fitting method, the subdomain is restricted to a domain of size $49 \times 36 \times 51$ voxels to include only one interface patch. Both types of cost functions are calculated at various experimental time steps t_n and are shown in Fig. 5. Notice here $\sqrt{f_{\mathrm{cost}}}$ of the norm-cost function is shown as it has a clear physical meaning. The norm-cost function (Eq. (3)) shows a smaller difference between fitting time steps t_n than the corr-cost function (Eq. (2)), as a result of the normalization. There is a well-defined minimum in all cases. At various time steps, the experimental microstructures and the simulated microstructures with three values of D^L represented by the three vertical lines in Fig. 5 are shown in Fig. 6. For visualization purposes, two slices are shown. We can see that when a small diffusion coefficient $D^L = 6 \times 10^{-10}\ m^2/s$ is used, the simulated interfaces move slower than the experimental ones. When a large diffusion coefficient $D^L = 1.8 \times 10^{-9}\ m^2/s$ is used, the opposite is observed. Only when the diffusion coefficient is near the optimal point $D^L = 1.3 \times 10^{-9}\ m^2/s$, we see a better match between experiment and simulation. Notice that the optimal value determined from the interface patch is a local fit and it can be different from a global fit. This will be discussed in section 3.4.2 and section 3.4.3.

3.4.2. Subdomain size study

To determine the size of a representative subdomain and study the influence of the external boundary, the fitting is performed using subdomains with an increasing size. Examples of cubic subdomains with different edge length k in units of grid points are shown in Fig. 7. The regions subject to the coalescence problem are removed from the fitting domain, see Appendix A for details. The resulting diffusion coefficients and the cost functions at the best fit are shown in Fig. 8. It is seen, that as more interface patches are included in the fitting domain, the fitted material parameter reaches a stable value for all four experimental time steps after $k = 160$. We interpret this to mean that interface area becomes statistically sufficient when $k > 160$. As the subdomain size continues to increase ($k > 250$), the influence of the boundary condition

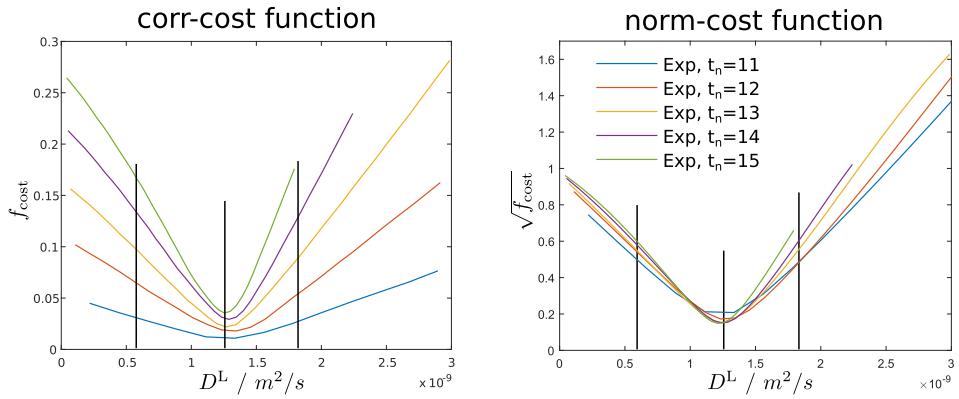

Fig. 5. The variation of the cost functions with D^{L} for the small interface patch at different experimental time steps t_n.

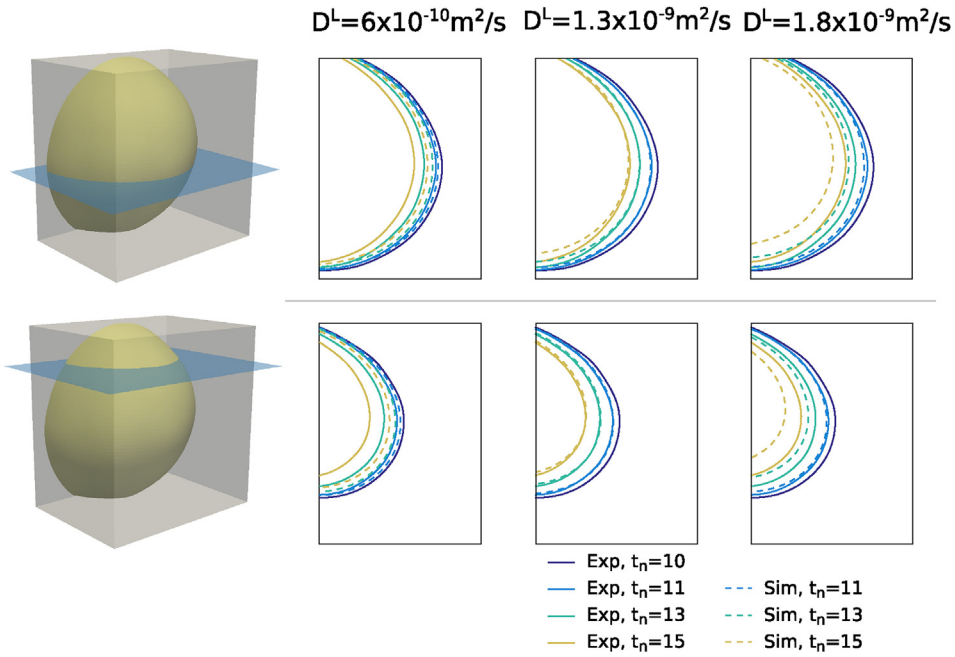

Fig. 6. Comparison between experimental and simulated microstructures of the small interface patch at different experimental time steps t_n.

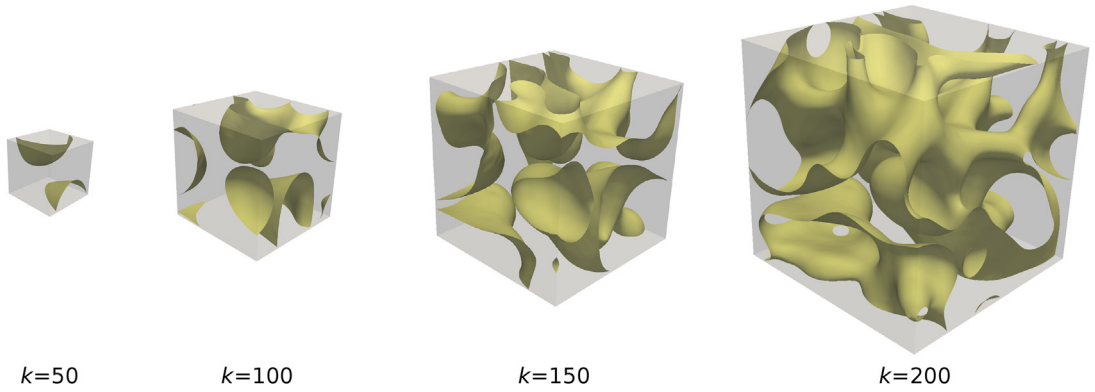

Fig. 7. Examples of subdomains with different sizes k.

starts to alter the fitted values. Simultaneously, as shown in Fig. 8(b), the cost functions start to increase near the boundary ($k > 250$), which means that the resulting diffusion coefficients are not correct. In summary, the influence of the boundary condition is around 25 to 50 grid points from the boundary. For the current problem, a subdomain with a size between $k = 160$ and $k = 210$ is

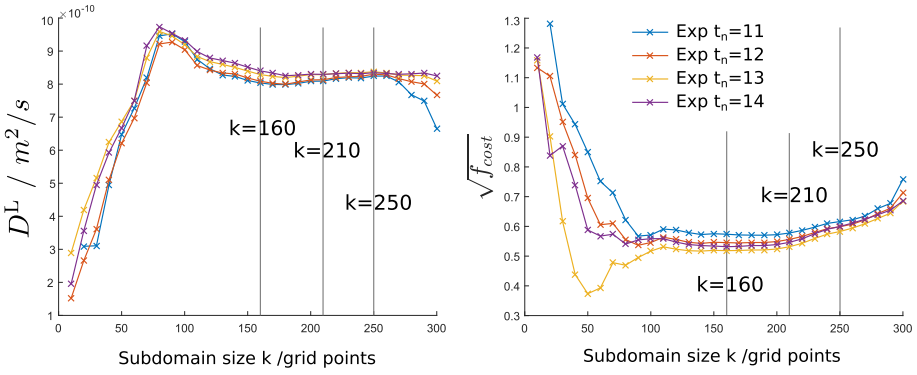

(a) The best-fit liquid diffusion coefficient (b) The cost function at the best fit

Fig. 8. Subdomain size study. Different curves are the fitting with different experimental time steps t_n.

called a representative subdomain. Here the values of time steps $t_n = 12, 13, 14$ are used (the time step 11 is not used to be consistent with section 3.4.4). The average of the 3×6 (three time steps and six representative subdomains) best-fit liquid diffusion coefficients is $8.21 \pm 0.12 \times 10^{-10}\ m^2/s$ with the indicated interval being the standard error.

3.4.3. Spatial variation of the fitted diffusion coefficients

In this section, subdomains with a fixed size but different locations within the simulation domain are studied. Using five subdomain sizes varying from $k = 50$ to $k = 150$, fitting is performed as the center of the subdomain sweeps through the entire simulation domain with a step of 10 grid points. The domain within 50 grid points from the simulation domain boundary is excluded because of the boundary condition (see section 3.4.2). The area of the interface within each subdomain is calculated and is plotted together with the fitted liquid diffusion coefficient in Fig. 9. As the surface area increases, there is a smaller spread of the points while the mean values of the distributions are similar for all subdomain sizes. As a result of the small step size, there will be overlap regions between subdomains; however, removing the overlapping regions reduces the density of points but does not change the overall trend in Fig. 9. Possible reasons for the spread of points include the influence of convection, temperature gradients in the sample, local impurity, reconstruction and segmentation errors and simulation errors. The convergence shown in Fig. 9 implies that the variation caused by these systematic errors is averaged out with increasing interface area. Hence we conclude that in the current system a large interface area is essential to average out local heterogeneity while fitting a limited number of representative subdomains is sufficient to get a high precision value of the material parameter.

3.4.4. Temporal variation of the fitted diffusion coefficients

As shown in Fig. 8, if we compare the resulting fitted diffusion coefficients of the representative subdomains at different fitting time steps t_n, they show a very small deviation.

Starting from different experimental time steps t_0, several phase-field simulations are performed, and the liquid diffusion coefficient D^L is fitted by comparing with three later experimental time steps $t^{exp} = t_0 + 2, 3, 4$ (the immediately followed time step $t_0 + 1$ is not used because the interfaces need time to move a sufficient distance). The six representative subdomains determined in section 3.4.2 are used for fitting. In total, 3×6 (three time steps and six representative subdomains) best-fit values of D^L are determined from the fitting. The mean value and standard deviation of these are shown as a function of t_0 in Fig. 10. We observe that the best-fit diffusion coefficient is nearly constant in time. Taking into account the variation in t_0, the fitted liquid diffusion coefficient is

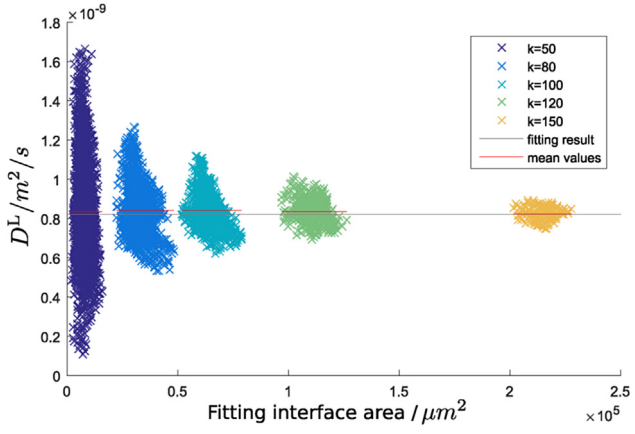

Fig. 9. Correlation between best-fit values of D^L and the fitting interface area for different subdomain size (fitting time $t_n = 12$). Points with the same color are results from the same subdomain size. The gray line shows the result of the fitting from the representative subdomains (section 3.4.2). The red lines show the mean value for each subdomain size. The scatter in the best-fit D^L decreases as the surface area increases. (For interpretation of the references to colour in this figure legend, the reader is referred to the web version of this article.)

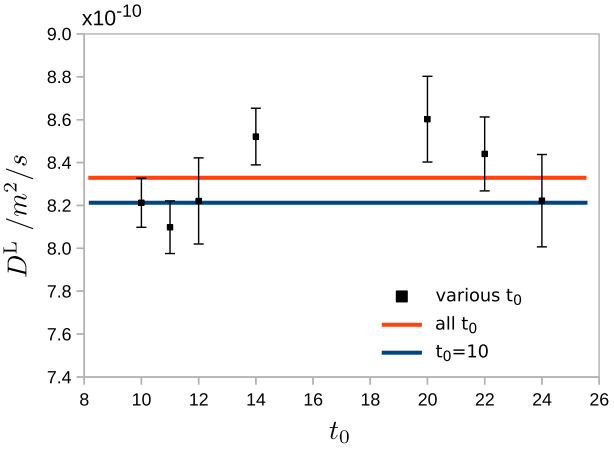

Fig. 10. Fitting results of different starting time steps t_0. The orange line shows the mean value determined from all t_0. The blue line shows the result determined from $t_0 = 10$, as given in section 3.4.2. (For interpretation of the references to colour in this figure legend, the reader is referred to the web version of this article.)

$8.33\pm0.24 \times 10^{-10}\ m^2/s$.

3.5. Two-parameters fitting: diffusion coefficient and capillary length

The fitting parameters are now the liquid diffusion coefficient and the capillary length $\mathbf{p} = \{D^L, l^L\}$. As the approach to determine the diffusion coefficient given in section 3.3 does not work for the capillary length, we need to perform a full phase-field simulation for each trial value of the capillary length. To reduce the computational cost, we here perform six phase-field simulations with six values of the capillary length. The liquid diffusion coefficient is fitted in a similar manner as in section 3.4 for each capillary length. The starting time step is $t_0 = 10$ and the fitting time step is $t_n = 12, 13, 14$. The size of representative subdomains is found to be between $k = 150$ and $k = 250$. The mean value and the standard deviation of the fitted liquid diffusion coefficients for each capillary length are determined with the representative subdomains. A linear fit as shown in Fig. 11 reveals that the best-fit values of D^L and l^L are not unique, but rather fulfill the relationship $D^L l^L = 0.518\pm0.011\ \mu m^3/s$ to good approximation. This is further substantiated by the values of the cost function at best-fit being indistinguishable within the fitting error. The observed relationship between the best-fit values of D^L and l^L is consistent with coarsening theory [53], and therefore indicates that the assumptions of the theory are correct.

4. Discussion

4.1. The fitting methodology

The results show that a consideration of statistics is important to get reliable fitted values of material parameters. Various error sources in experiment, simulation, and fitting may cause a large scatter of the locally fitted values. This, on the one hand, indicates that the local measurement of material parameters, which traditional techniques rely on, can be questionable. On the other hand, the amount of interface involved in the fitting methodology introduced here needs to be statistically sufficient to make sure the local variation is averaged out.

A good cost function should help extract useful information from the experimental data while being insensitive to noise. The corr-cost function (Eq. (2)) is easy to calculate, but when the geometry is represented by a limited number of voxels, there will be discontinuities in the cost function. The norm-cost function (Eq. (3)) is continuous, but an extra effort is needed to generate the signed distance function. Generally speaking, both cost functions work equally well in the case investigated here.

Though in this paper we apply the proposed fitting methodology to coarsening of a binary system, we foresee it can be applied to more complex material systems and physical processes, for example:

1. Systems with more than two phases and/or components: measure e.g. the interdiffusion coefficients in a multicomponent system and the anisotropic grain boundary energies/mobilities and the triple junction mobilities of a polycrystalline material.
2. Processes other than coarsening: measure e.g. the mobilities of domain walls in ferroelectric/piezoelectric materials and the dislocation mobility in crystalline materials.
3. Materials with structural hierarchy: determine material parameters which have an influence across scales with the help of multiscale experimental and modeling techniques.

The fitting methodology is also a very powerful way to provide insight on the quality of the materials model. If the result of the optimization is a poor global match between experiment and optimized model, it may indicate that one or more mechanisms are absent from the model. If the simulation only deviates from the experiment in a local region, we may either attempt to improve the underlying model or exclude the problematic regions. Our work shows that in the case of coarsening we can get good results with the simplified model and a fitting domain excluding the problematic regions.

Applying the proposed method to fitting more than one independent material parameters is straightforward by using multivariable optimization algorithms. The main limitation of the fitting methodology is the heavy computational cost as generally the phase-field simulation need to be performed many times. For the case investigated here, the phase-field simulations for one experimental time step with a 300^3 domain took 22 h on a Nehalem architecture machine with 16 cores and took 11 h for simulations with a 400^3 domain on a Sandy Bridge architecture machine with 64 cores. However, the simulations may be speeded up by massively parallel computing and fast convergence optimization algorithms, and a good initial guess of the material parameters will shorten the path to the global minimum. Furthermore, we anticipate that in many cases it will be sufficient to base the fitting of some of the parameters on small regions in space-time.

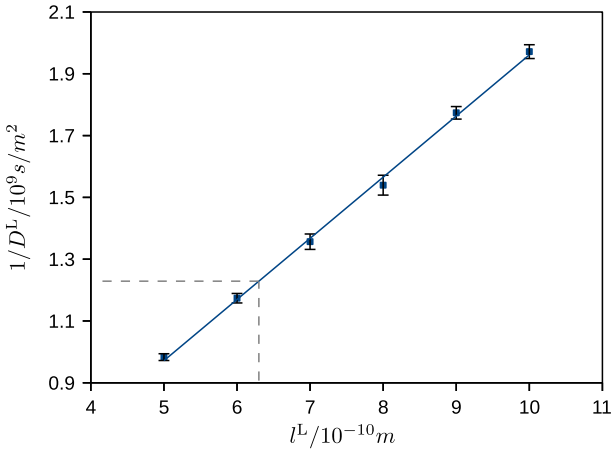

Fig. 11. The optimal values of the liquid diffusion coefficient D^L and the capillary length l^L. The blue line shows a linear fit to the points. The error bar is calculated from the representative subdomains. The dotted lines show l^L used in the one-parameter fitting and the corresponding D^L.

4.2. The Al-Cu alloy

The liquid diffusion coefficient of the hypo-eutectic Al-Cu has been experimentally measured several times [24,33–35], resulting in a large scatter of values between $\sim 8 \times 10^{-10}\ m^2/s$ and $\sim 6 \times 10^{-9}\ m^2/s$. Except for the value determined by Aagesen et al. [24]: $D^L = 8.3 \times 10^{-10}\ m^2/s$, the previously reported values are larger than the one determined in this paper. The most popular technique to measure the liquid diffusion coefficient employs a capillary tube. As shown by Lee et al. [33], convection in the liquid is not negligible in a capillary tube experiment if the diameter of the tube is large and this will result in a larger measured liquid diffusion coefficient. In that work, the liquid diffusion coefficient is measured during directional solidification, and the capillary tube diameter is chosen to be small ($< 0.8\ mm$) to minimize the effect of convection, but it is not clear that convection had been eliminated as a source of bias. In Aagesen et al. [24] and in the current study, the features of the microstructures are at a micrometer scale so the

Rayleigh number is very small; hence convection can be neglected. The experiment is also isothermal, unlike experiments that determine diffusion coefficients by composition measurements on quenched samples following directional solidification where a large temperature gradient is present, e.g. 10 K/mm in Ref. [33]. This can result in an uncertainty in the temperature and composition at which the liquid diffusion coefficient is determined. Moreover, microstructure evolution during quench may alter the composition profile, which is prevented in the present study since the measurements are in situ. Compared to the liquid diffusion coefficient, the measured values of the capillary length show small scatter [31,32]. The capillary length used in the one-parameter fitting is calculated from the Gibbs-Thomson coefficient measured by Gündüz and Hunt [31] in the grain boundary groove experiments. Given this value of the capillary length, the measured liquid diffusion coefficient from the one-parameter fitting has a value of $D^{\mathrm{L}} = 8.33\pm0.24 \times 10^{-10}\ m^2/s$. Taking into account the uncertainty in the measurement of the Gibbs-Thomson coefficient ($5\% \sim 7\%$) [31,32], we have $D^{\mathrm{L}} = 8.3\pm0.9 \times 10^{-10}\ m^2/s$ by assuming linear error propagation.

5. Conclusion

We have developed a methodology of fitting material parameters by comparison between time-resolved 3D experimental measurements of microstructure and simulations. Compared to traditional ways of material parameter measurement, samples and sample environments representative of bulk properties and actual processing conditions can be used and several parameters can be fitted simultaneously. The fitting methodology was presented with subsequent discussions on the cost functions, the fitting domain, and the statistics. As a demonstration, our methodology is applied to a hypo-eutectic Al-Cu system to determine the liquid diffusion coefficient and the capillary length. A detailed analysis of the fitting is given, including the convergence over subdomain size/interface area and the temporal and the spatial variation of the fitted values. From simulations varying both diffusion coefficient and liquid capillary length, it is found that the best-fit values are not unique, but are found to fulfill $D^{\mathrm{L}}l^{\mathrm{L}} = 0.518\pm0.011\ \mu m^3/s$ which corroborates a basic hypothesis of the coarsening theory. Given the value of the capillary length, the measured liquid diffusion coefficient from the one-parameter fitting has a value of $D^{\mathrm{L}} = 8.33\pm0.24 \times 10^{-10}\ m^2/s$. The proposed fitting methodology provides a way to measure microstructure material parameters which are difficult to be measured by traditional methods.

Acknowledgment

JZ and HFP acknowledge the financial support of the CINEMA project. SOP acknowledges financial assistance award 70NANB14H012 from U.S. Department of Commerce, National Institute of Standards and Technology as part of the Center for Hierarchical Materials Design (CHiMaD). HFP acknowledges the ERC advanced grant d-TXM. The usage of supercomputers Quest at Northwestern University and Niflheim at Technical University of Denmark is acknowledged. JZ thanks Yue Sun and Matthew Peters at Northwestern University for helpful discussion.

Appendix A. Elimination of the coalescence regions

As the thin liquid films sometimes observed separating solid particles in the experiment, see Fig. 4, are too thin to be resolved in the phase-field simulation, interfaces close to each other in the simulations will tend to coalesce. Regions where this happens should be removed from the fitting domain to get a reliable fitted value of material parameters. A common feature of those regions is that the interface has very high velocity. Here the high-velocity domains are selected and then removed from Ω_{fit} with a given velocity threshold v_{min} by

$$\Omega_{\mathrm{highv}} = \{\mathbf{x} : |\mathbf{v}(\mathbf{x})| \geqslant v_{\mathrm{min}}\} \tag{A.1}$$

The coalescence may influence the evolution of interfaces nearby, so a dilation of the high-velocity region is performed to include nearby regions. The velocity threshold and the extent of dilation are chosen to ensure that the influence on the fitting result is minimized.

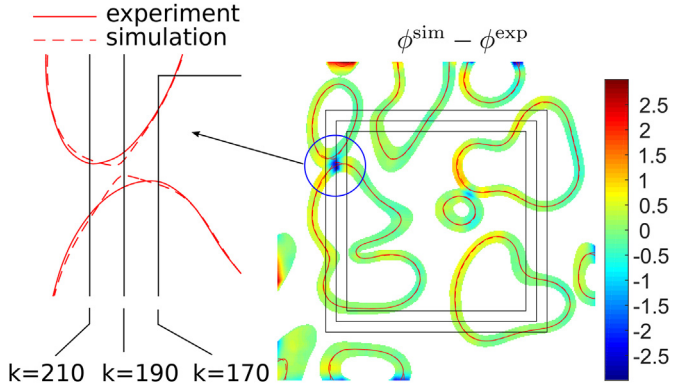

Fig. A.12. In coalescence regions, there is a large difference between ϕ^{exp} and ϕ^{sim}, indicating a large velocity. The square boxes show the subdomains with different sizes k.

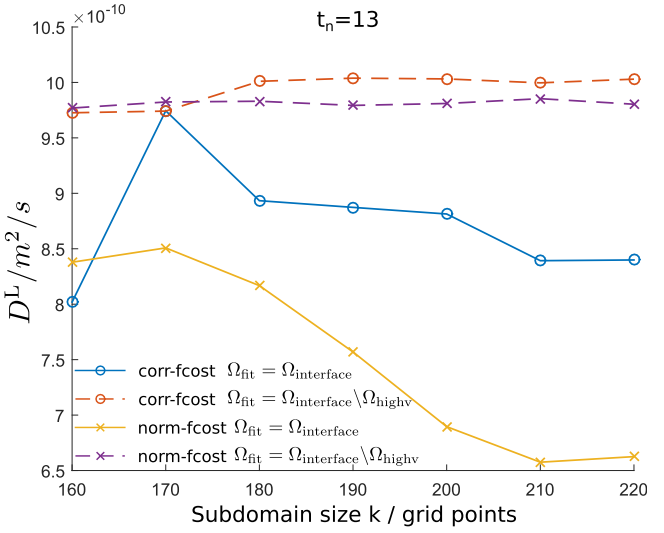

Fig. A.13. Influence of the high-velocity region Ω_{highv}. Solid and dashed lines are fitting results with and without Ω_{highv}, respectively. Lines with circular and cross symbols are fitting results using the corr-cost function (Eq. (2)) and the norm-cost function (Eq. (3)), respectively.

The influence of the high-velocity regions on the fitting results is shown by a simplified problem. For visualization purposes, the fitting domain is a 2D slice of a 3D simulation domain. We can see a coalescence event inside subdomain of size $k = 210$ but not $k = 170$. The value $(\phi^{\mathrm{sim}} - \phi^{\mathrm{exp}})/\Delta t$ can be regarded as the interfacial velocity and is shown in Fig. A.12 (right). For simplicity, here Δt is set to be one and the signed distance functions have a unit of grid points. The magnitude of $\phi^{\mathrm{sim}} - \phi^{\mathrm{exp}}$ is very large in the coalescence region compare to the other regions. The fitted values of the liquid diffusion coefficient are plotted with the subdomain sizes in Fig. A.13. When the fitting is performed with the high-velocity regions, the best-fit D^{L} will be underestimated as the high-

velocity interfaces tend to dominate the fitting result. So as more high-velocity regions are included in fitting, the best-fit values decrease, as shown by the solid lines in Fig. A.13. The fitted values with a fitting domain eliminating the high-velocity region (dashed lines) show a smaller scatter than the ones with the high-velocity region (solid lines) and show a similar best-fit value for both cost functions. We conclude that the proposed process excludes regions of the simulations where coalescence occurs without biasing the global fit.

References

[1] G.B. Olson, Computational design of hierarchically structured materials, Science 277 (1997) 1237–1242.
[2] National Research Council, Integrated Computational Materials Engineering: a Transformational Discipline for Improved Competitiveness and National Security, The National Academies Press, Washington, DC, 2008, http://dx.doi.org/10.17226/12199.
[3] OSTP, Materials Genome Initiative for Global Competitiveness, Technical Report, Office of Science and Technology Policy, Washingtom, DC, 2011. URL: https://www.whitehouse.gov/sites/default/files/microsites/ostp/materials_genome_initiative-final.pdf.
[4] G. Olson, C. Kuehmann, Materials genomics: from CALPHAD to flight, Scr. Mater 70 (2014) 25–30.
[5] Z.-K. Liu, First-principles calculations and CALPHAD modeling of thermodynamics, J. Phase Equilib. Diffus. 30 (2009) 517–534.
[6] M. Mantina, Y. Wang, R. Arroyave, L.Q. Chen, Z.K. Liu, C. Wolverton, First-principles calculation of self-diffusion coefficients, Phys. Rev. Lett. 100 (2008) 215901.
[7] M. Mantina, S.L. Shang, Y. Wang, L.Q. Chen, Z.K. Liu, 3*d* transition metal impurities in aluminum: a first-principles study, Phys. Rev. B 80 (2009) 184111.
[8] B.-C. Zhou, S.-L. Shang, Y. Wang, Z.-K. Liu, Diffusion coefficients of alloying elements in dilute Mg alloys: a comprehensive first-principles study, Acta Mater 103 (2016) 573–586.
[9] W. Wang, H. Fang, S. Shang, H. Zhang, Y. Wang, X. Hui, S. Mathaudhu, Z. Liu, Atomic structure and diffusivity in liquid Al_{80} Ni_{20} by ab initio molecular dynamics simulations, Phys. B 406 (2011) 3089–3097.
[10] M. Strobl, I. Manke, N. Kardjilov, A. Hilger, M. Dawson, J. Banhart, Advances in neutron radiography and tomography, J. Phys. D. Appl. Phys. 42 (2009) 243001.
[11] E. Maire, P.J. Withers, Quantitative x-ray tomography, Int. Mater. Rev. 59 (2014) 1–43.
[12] H.F. Poulsen, Three-dimensional X-ray Diffraction Microscopy: Mapping Polycrystals and Their Dynamics, Volume 205 of Springer Tracts in Modern Physics, Springer Berlin Heidelberg, 2004, http://dx.doi.org/10.1007/b97884.
[13] W. Ludwig, S. Schmidt, E.M. Lauridsen, H.F. Poulsen, X-ray diffraction contrast tomography: a novel technique for three-dimensional grain mapping of polycrystals. I. direct beam case, J. Appl. Crystallogr. 41 (2008) 302–309.
[14] D.J. Rowenhorst, P.W. Voorhees, Measurement of interfacial evolution in three dimensions, Annu. Rev. Mater. Res. 42 (2012) 105–124.
[15] C. Raufaste, B. Dollet, K. Mader, S. Santucci, R. Mokso, Three-dimensional foam flow resolved by fast x-ray tomographic microscopy, Europhys. Lett. 111 (2015) 38004.
[16] S. McDonald, P. Reischig, C. Holzner, E. Lauridsen, P. Withers, A. Merkle, M. Feser, Non-destructive mapping of grain orientations in 3D by laboratory x-ray microscopy, Sci. Rep. 5 (2015) 14665.
[17] A. Karma, W.-J. Rappel, Quantitative phase-field modeling of dendritic growth in two and three dimensions, Phys. Rev. E 57 (1998) 4323–4349.
[18] A. Karma, Phase-field formulation for quantitative modeling of alloy solidification, Phys. Rev. Lett. 87 (2001) 115701.
[19] N. Moelans, A quantitative and thermodynamically consistent phase-field interpolation function for multi-phase systems, Acta Mater 59 (2011) 1077–1086.
[20] I. Steinbach, Phase-field model for microstructure evolution at the mesoscopic scale, Annu. Rev. Mater. Res. 43 (2013) 89–107.
[21] D. Zöllner, P. Streitenberger, Three-dimensional normal grain growth: Monte Carlo Potts model simulation and analytical mean field theory, Scr. Mater 54 (2006) 1697–1702.
[22] M. Syha, D. Weygand, A generalized vertex dynamics model for grain growth in three dimensions, Modell. Simul. Mater. Sci. Eng. 18 (2010) 015010.
[23] S. Chen, B. Merriman, S. Osher, P. Smereka, A simple level set method for solving stefan problems, J. Comput. Phys. 135 (1997) 8–29.
[24] L.K. Aagesen, J.L. Fife, E.M. Lauridsen, P.W. Voorhees, The evolution of interfacial morphology during coarsening: a comparison between 4D experiments and phase-field simulations, Scr. Mater 64 (2011) 394–397.
[25] I.M. McKenna, S.O. Poulsen, E.M. Lauridsen, W. Ludwig, P.W. Voorhees, Grain growth in four dimensions: a comparison between simulation and experiment, Acta Mater 78 (2014) 125–134.
[26] M. Wang, Y. Xu, Q. Zheng, S. Wu, T. Jing, N. Chawla, Dendritic growth in Mg-based alloys: phase-field simulations and experimental verification by x-ray synchrotron tomography, Metall. Mater. Trans. A 45 (2014) 2562–2574.
[27] P. Steinmetz, Y.C. Yabansu, J. Hötzer, M. Jainta, B. Nestler, S.R. Kalidindi, Analytics for microstructure datasets produced by phase-field simulations, Acta Mater 103 (2016) 192–203.
[28] M.C. Demirel, A.P. Kuprat, D.C. George, A.D. Rollett, Bridging simulations and experiments in microstructure evolution, Phys. Rev. Lett. 90 (2003) 016106.
[29] I. Ansara, A.T. Dinsdale, M.H. Rand (Eds.), COST 507: Thermochemical Database for Light Metal Alloys, vol. 2, European Commission, Directorate-General XII, Science, Research and Development, 1998.
[30] V. Witusiewicz, U. Hecht, S. Fries, S. Rex, The Ag-Al-Cu system: Part I: reassessment of the constituent binaries on the basis of new experimental data, J. Alloys Compd. 385 (2004) 133–143.
[31] M. Gündüz, J. Hunt, The measurement of solid-liquid surface energies in the Al-Cu, Al-Si and Pb-Sn systems, Acta Metall. 33 (1985) 1651–1672.
[32] N. Maraşli, J. Hunt, Solid-liquid surface energies in the Al-$CuAl_2$, Al-$NiAl_3$ and Al-Ti systems, Acta Mater 44 (1996) 1085–1096.
[33] J.-H. Lee, S. Liu, H. Miyahara, R. Trivedi, Diffusion-coefficient measurements in liquid metallic alloys, Metall. Mater. Trans. B 35 (2004) 909–917.
[34] U. Dahlborg, M. Besser, M. Calvo-Dahlborg, S. Janssen, F. Juranyi, M. Kramer, J. Morris, D. Sordelet, Diffusion of Cu in AlCu alloys of different composition by quasielastic neutron scattering, J. Non-Cryst. Solids 353 (2007) 3295–3299.
[35] B. Zhang, A. Griesche, A. Meyer, Diffusion in Al-Cu melts studied by time-resolved x-ray radiography, Phys. Rev. Lett. 104 (2010) 035902.
[36] L. Piegl, W. Tiller, The NURBS Book, Springer-Verlag Berlin Heidelberg, 1995, http://dx.doi.org/10.1007/978-3-642-97385-7.
[37] J.A. Sethian, Level Set Methods and Fast Marching Methods: Evolving Interfaces in Computational Geometry, Fluid Mechanics, Computer Vision, and Materials Science, vol. 3, Cambridge University Press, 1999.
[38] J.W. Gibbs, P.W. Voorhees, Segmentation of four-dimensional, x-ray computed tomography data, Integr. Mater. Manuf. Innov. 3 (2014) 1–12.
[39] G. Russo, P. Smereka, A remark on computing distance functions, J. Comput. Phys. 163 (2000) 51–67.
[40] J.W. Gibbs, Interfacial Dynamics in Liquid-solid Mixtures: a Study of Solidification and Coarsening, Ph.D. thesis, Northwestern University, 2014.
[41] J.L. Fife, Three-dimensional Characterization and Real-time Interface Dynamics of Aluminum-copper Dendritic Microstructures, Ph.D. thesis, Northwestern University, 2009.
[42] J.W. Gibbs, P.W. Voorhees, J.L. Fife, Dataset for Segmentation of Four-dimensional, X-ray Computed Tomography Data, 2016, http://dx.doi.org/10.18126/M2CC73.
[43] L.-Q. Chen, W. Yang, Computer simulation of the domain dynamics of a quenched system with a large number of nonconserved order parameters: the grain-growth kinetics, Phys. Rev. B 50 (1994) 15752–15756.
[44] I. Steinbach, F. Pezzolla, B. Nestler, M. Seeßelberg, R. Prieler, G. Schmitz, J. Rezende, A phase field concept for multiphase systems, Phys. D. 94 (1996) 135–147.
[45] S.G. Kim, W.T. Kim, T. Suzuki, Interfacial compositions of solid and liquid in a phase-field model with finite interface thickness for isothermal solidification in binary alloys, Phys. Rev. E 58 (1998) 3316–3323.
[46] S.G. Kim, A phase-field model with antitrapping current for multicomponent alloys with arbitrary thermodynamic properties, Acta Mater 55 (2007) 4391–4399.
[47] N. Moelans, B. Blanpain, P. Wollants, Quantitative analysis of grain boundary properties in a generalized phase field model for grain growth in anisotropic systems, Phys. Rev. B 78 (2008) 024113.
[48] N. Provatas, K. Elder, Phase-field Methods in Materials Science and Engineering, John Wiley & Sons, 2011, http://dx.doi.org/10.1002/9783527631520.
[49] S. Liu, R. Napolitano, R. Trivedi, Measurement of anisotropy of crystal-melt interfacial energy for a binary Al-Cu alloy, Acta Mater 49 (2001) 4271–4276.
[50] L.K. Aagesen, Phase-field Simulation of Solidification and Coarsening in Dendritic Microstructures, Ph.D. thesis, Northwestern University, 2010.
[51] B. Echebarria, R. Folch, A. Karma, M. Plapp, Quantitative phase-field model of alloy solidification, Phys. Rev. E 70 (2004) 061604.
[52] A. Karma, W.-J. Rappel, Phase-field method for computationally efficient modeling of solidification with arbitrary interface kinetics, Phys. Rev. E 53 (1996) R3017–R3020.
[53] L. Ratke, P.W. Voorhees, Growth and Coarsening: Ostwald Ripening in Material Processing, Springer Science & Business Media, 2002.